JOURNAL OF COMPUTATIONAL PHYSICS **138,** 617–643 (1997)
ARTICLE NO. CP975836

Optimized Compact-Difference-Based Finite-Volume Schemes for Linear Wave Phenomena

Datta Gaitonde*,[1] and J. S. Shang†

WL/FIMC, Building 450, 2645 Fifth Street, Suite 7, Wright–Patterson AFB, Ohio 45433-7913
E-mail: *datta†shang@fim.wpafb.af.mil

Received February 17, 1997; revised August 28, 1997

High-order compact-difference-based finite-volume schemes are developed, analyzed, and implemented for linear wave propagation phenomena with particular emphasis on computational electromagnetics in the time-domain. The formulation combines the primitive function approach with five-point spatially sixth- and fourth-order methods. Optimization in the semi-discrete case is achieved by minimizing dispersion and isotropy error. The fully discrete scheme is examined by adopting the classical fourth-order Runge–Kutta technique. Stability bounds are established and the coefficients for the spatial discretization are readjusted for optimum performance. The scheme is then formally extended to multiple dimensions. Consistent boundary conditions are presented for the reconstruction operator as well as flux specification. Several calculations in one and three dimensions confirm the properties of the method.

Key Words: high-order; finite volume; electromagnetics; compact differencing.

1. INTRODUCTION

The integration of Maxwell's equations in the time-domain is a computationally intensive endeavor. Present production algorithms for computational electromagnetics (CEM) are generally second- or third-order accurate (see, e.g., Refs. [1–3]). A previous effort [3] has described the implementation of the *MUSCL* family of up to third-order schemes for CEM problems. The formulation is derived from characteristic theory which describes the solution in terms of left and right running wave components. In this approach, the ''left'' and ''right'' states of the solution

[1] Corresponding author. OAI (ICOMP).

0021-9991/97 $25.00

vector are first derived at each cell boundary in the domain. The interface flux is then computed through eigenvalue-based splitting and the solution is advanced in time with a two-stage second-order Runge–Kutta scheme. The method is robust but is relatively diffusive and dispersive at low and high CFL numbers, respectively. It is thus unsuitable for problems requiring long-time integration. For example, the radar cross section (RCS) calculation of a typical fighter aircraft under gigahertz excitation will require $O(10^5)$ single-processor hours on a Cray C90 and $O(10^{12})$ words of memory. More accurate spatial and temporal methods are potentially more efficient because fewer mesh points and time steps will be required.

Centered schemes have recently gained much popularity in the simulation of wave propagation phenomena [4–7]. In contrast to upwind methods, the dominant error in centered semi-discretizations is dispersive. Of particular interest has been a subset of centered schemes which require very small stencil support. These ''compact'' schemes can be derived from Taylor series expansions and compute derivatives in a coupled fashion along an entire line. Such methods have the advantage of simpler boundary condition treatment than their noncompact counterparts and in addition have smaller truncation error [8].

Compact-difference schemes have been implemented primarily in the finite-difference (FD) formulation which is relatively straightforward to extend to multiple dimensions and to generalized coordinates. The incorporation of compact-difference schemes into the finite-volume (FV) formulation is more complex and, thus, has lagged significantly in its development. FV methods have several advantages—for nonlinear phenomena an extensive comparison with high-order FD methods may be found in Ref. [9]. In FV, since the fluxes collapse telescopically by construction, flux conservation is easily enforced even on arbitrary meshes. Further, analyses of cell-centered-type approaches arising naturally in FV are known to have superior performance in the high wave number range [4] and, also, exhibit lower truncation error [10]. For these reasons, the present effort will focus on the introduction of compact-difference schemes to the FV methodology as described in Sections 2.1 and 2.2.

The tridiagonal-based five-point spatial discretization operator chosen in this work yields a unique sixth-order scheme (Section 2.3). However, through an optimization procedure for the same stencil and thus computational effort, lower order schemes can be devised to achieve superior performance in the high wave number range than the formally sixth-order scheme. Some optimization techniques may be found in Refs. [4–7]. A single parameter continuous spectrum of fourth-order optimized schemes is developed in Section 2.4. The high-order reconstruction step is illustrated in Section 2.5 which also includes a determination of semi-discrete order of accuracy.

The dynamic nature of electromagnetic wave propagation necessitates the use of accurate time integration methods as well. Since a frequency dependent time-step size restriction usually exists from accuracy considerations, contemporary methods are generally explicit [1–3]. The classical single-step multistage Runge–Kutta method of fourth-order accuracy, RK4 is chosen for the present effort (Section 3). This scheme has a relatively large stability bound and can be implemented very efficiently [11]. In Section 4, the full discretization with RK4 is examined and the

optimization coefficients for spatial discretization are adjusted further as functions of the Courant number, ν.

Much of the scheme development is performed in the context of the scalar advection equation. The formal high-order extension to systems of equations in multiple dimensions is described in Section 5. The implementation of boundary conditions is outlined in Section 6. Section 7 concludes the paper with simple but illustrative examples utilizing periodic as well as nonperiodic boundary conditions.

2. DESCRIPTION AND ANALYSIS OF SCHEME

2.1. *Finite-Volume Formulation*

The time dependent Maxwell's equations for an electromagnetic field in free space can be written in flux vector form on a Cartesian (x, y, z) frame as [12, 13]

$$\frac{\partial U}{\partial t} + \frac{\partial \mathfrak{F}}{\partial x} + \frac{\partial \mathfrak{G}}{\partial y} + \frac{\partial \mathfrak{H}}{\partial z} = -J, \quad \text{or} \quad \frac{\partial U}{\partial t} + \nabla \cdot \Xi = -J, \tag{1}$$

where the solution vector U is written in terms of the electric and magnetic field strengths, E and H, respectively, as $U = [E_x, E_y, E_z, H_x, H_y, H_z]^{\mathrm{T}}$. $\mathfrak{F}$, $\mathfrak{G}$, and $\mathfrak{H}$ are the flux vectors:

$$\mathfrak{F} = \begin{Bmatrix} 0 \\ H_z/\varepsilon \\ -H_y/\varepsilon \\ 0 \\ -E_z/\mu \\ E_y/\mu \end{Bmatrix}, \quad \mathfrak{G} = \begin{Bmatrix} -H_z/\varepsilon \\ 0 \\ H_x/\varepsilon \\ E_z/\mu \\ 0 \\ -E_x/\mu \end{Bmatrix}, \quad \mathfrak{H} = \begin{Bmatrix} H_y/\varepsilon \\ -H_x/\varepsilon \\ 0 \\ -E_y/\mu \\ E_x/\mu \\ 0 \end{Bmatrix} \tag{2}$$

while Ξ is the point flux tensor $(\mathfrak{F}i + \mathfrak{G}j + \mathfrak{H}k)$. J is the source vector $[J_x/\varepsilon, J_y/\varepsilon, J_z/\varepsilon, 0, 0, 0]^{\mathrm{T}}$. For the present investigation, the propagating waves are assumed to be confined in isotropic media separated by physical interfaces. Under these conditions, the permittivity, ε, and permeability, μ, are assumed constant but have different values in various media [12, 13].

To develop the FV formulation, Eq. (1) is integrated over a volume, $\mathbb{V}$:

$$\iiint_{\mathbb{V}} \frac{\partial U}{\partial t}\, d\mathbb{V} + \iiint_{\mathbb{V}} \nabla \cdot \vec{\Xi}\, d\mathbb{V} = -\iiint_{\mathbb{V}} J\, d\mathbb{V}. \tag{3}$$

With the application of the Gauss divergence theorem, Eq. (3) becomes

$$\frac{\partial \mathbb{V}\overline{\overline{U}}}{\partial t} + \iint_S \Xi \cdot n\, ds = -\mathbb{V}\overline{\overline{J}}, \tag{4}$$

where n is the directed area vector on the surface, S, bounding $\mathbb{V}$, and the overbarred

quantities represent cell averages; *e.g.*, $\overline{\overline{\overline{U}}} = (1/\mathbb{V}) \int\int_{\mathbb{V}}\int U$. Equation (4) relates the evolution of the cell average to the boundary fluxes which are functions of the pointwise values of U on the bounding surface. Therefore, for any cell c comprised of N surfaces with outward normals S_n,

$$\frac{\partial \mathbb{V} \overline{\overline{\overline{U}}}_c}{\partial t} + \Sigma_{n=1}^{N} \overline{\overline{\Xi}} \cdot S_n = \overline{\overline{J}}_c. \tag{5}$$

In discrete form, with $\hat{}$ denoting the discrete approximate of each quantity, Eq. (5) becomes

$$\frac{\Delta \mathbb{V} \hat{\overline{\overline{\overline{U}}}}_c}{\Delta t} + \Sigma_{n=1}^{N} \hat{\overline{\overline{\Xi}}} \cdot S_n = \hat{\overline{\overline{J}}}_c. \tag{6}$$

Flux conservation is enforced by determining a unique flux for each face as described below.

The 1D advection equation is used as the prototype for scheme development:

$$\frac{\partial u}{\partial t} + \frac{\partial f}{\partial x} = 0, \quad f = cu, \quad c > 0. \tag{7}$$

For a control volume, $x - h/2 < x < x + h/2$, Eq. (5) then implies

$$\frac{\partial h\overline{u}}{\partial t} + \left[f\left(u\left(x + \frac{h}{2}, t\right)\right) - f\left(u\left(x - \frac{h}{2}, t\right)\right)\right] = 0, \tag{8}$$

where $\overline{u}$ denotes again the average value of u, $\overline{u} = (1/h) \int_{x-h/2}^{x+h/2} u\, dx$. A mesh is introduced in the domain $0 < x < L$ consisting of N cells denoted 1, 2, ..., i, ..., N, and $N + 1$ interfaces, $\frac{1}{2}, \frac{3}{2}, ..., i - \frac{1}{2}, i + \frac{1}{2}, ..., N + \frac{1}{2}$, as shown in Fig. 1. The discrete approximation of Eq. (8) is then

$$\frac{\partial \hat{\overline{u}}_i}{\partial t} + \frac{1}{h}[\hat{f}_{i+1/2} - \hat{f}_{i-1/2}] = 0, \tag{9}$$

where $\hat{f}$ is the flux function approximating f:

$$\hat{f}_{i+1/2} = \hat{f}(..., \hat{\overline{u}}_{i-1}, \hat{\overline{u}}_i, \hat{\overline{u}}_{i+1}, ...) = \hat{f}(\hat{u}_{i+1/2}). \tag{10}$$

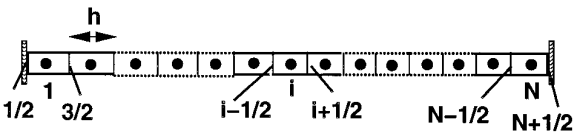

FIG. 1. Notation for 1D mesh.

The order of accuracy can now be introduced into the formulation in the manner of Ref. [14], where it is shown that for smooth solutions and focusing on the semi-discrete case, if

$$\hat{f}(\hat{u}_{i+1/2}) = f(u_{i+1/2}) + O(h^n) \tag{11}$$

then

$$\hat{\bar{u}}_i = \bar{u}_i + O(h^n). \tag{12}$$

In practical terms, knowing $\hat{\bar{u}}_i$, a crucial step *reconstruction* consists of approximating the pointwise quantity $\hat{u}_{i+1/2}$ to the desired accuracy to enforce Eq. (11); *i.e.,* the problem is to determine

$$\hat{u}_{i+1/2} = u_{i+1/2} + O(h^n). \tag{13}$$

2.2. *Reconstruction*

The first step in reconstruction is to form a primitive function as in Ref. [14]. The primitive function $\mathscr{V}$ of u is defined as $\mathscr{V} = \int_0^x u\,dx$. By the second fundamental theorem of calculus, $d\mathscr{V}/dx = u(x)$. In the discrete case,

$$\hat{\mathscr{V}}_{1/2} = 0; \quad \hat{\mathscr{V}}_{i+1/2} = \hat{\mathscr{V}}_{i-1/2} + \hat{\bar{u}}_i h, \quad i = 1, ..., N, \tag{14}$$

which follows from the definitions of $\mathscr{V}$ and $\hat{\bar{u}}$ and where $\hat{\mathscr{V}}_{1/2}$ is set to zero arbitrarily without loss of generality. From the analysis of Ref. [14] for smooth solutions the desired pointwise values of $\hat{u}_{i+1/2}$ may be obtained by evaluating $d\hat{\mathscr{V}}/dx$:

$$\hat{u}_{i+1/2} = \frac{d\hat{\mathscr{V}}}{dx} + O(h^n) = u_{i+1/2} + O(h^n). \tag{15}$$

In the following, only discretized quantities are considered and the $\hat{}$ is suppressed for simplicity. At this stage, the present approach deviates from the essentially nonoscillatory (ENO) scheme described in Refs. [14, 15]. A five-point compact stencil is employed to evaluate $\mathscr{V}' = d\mathscr{V}/dx (= u)$ at each interface,

$$\alpha\mathscr{V}'_{i-1/2} + \mathscr{V}'_{i+1/2} + \alpha\mathscr{V}'_{i+3/2} = b\,\frac{\mathscr{V}_{i+5/2} - \mathscr{V}_{i-3/2}}{4h} + a\,\frac{\mathscr{V}_{i+3/2} - \mathscr{V}_{i-1/2}}{2h}, \tag{16}$$

where α, a, and b are constants which determine the spatial properties of the algorithm. Equation (16) represents a tridiagonal equation system if $\alpha \neq 0$. In FD settings, similar stencils have been employed, for example, in Refs. [4, 6, 7, 16].

2.3. *Semi-discrete Analysis of Compact Differencing Scheme*

Upon inserting Taylor series expansions of each term in Eq. (16) about point

TABLE I
Classification of Schemes Based on Semidiscrete Optimization

Scheme	α	OA	TE
MUSCL	—	3	$h^3 \frac{f^{(4)}}{12}$
E4	0	4	$-h^4 \frac{f^{(5)}}{30}$
CD4	$\frac{1}{4}$	4	$-h^4 \frac{f^{(5)}}{120}$
CD6	$\frac{1}{3}$	6	$h^6 \frac{f^{(7)}}{1260}$
CD4O1	0.347485	4	$h^4 \left(\frac{-f^{(5)}}{30} + \frac{\alpha f^{(5)}}{10} \right)$
CD4O2	0.351075	4	–do–
CD4O3	0.370733	4	–do–
CD4O4	0.381365	4	–do–
CD4O5	0.430816	4	–do–
CD4O6	0.376374	4	–do–
CD4O7	0.400218	4	–do–

Note. $a = 2(2 + \alpha)/3$, $b = (-1 + 4\alpha)/3$, $f^{(n)} = \partial f^n / \partial x^n$; OA = order of accuracy, TE = leading term in truncation error.

$i + 1/2$, and matching coefficients of the various orders, the following sequence of equations is obtained:

$$\begin{aligned} O(h^2): &\quad 1 - a + 2\alpha - b = 0 \\ O(h^4): &\quad -a + 6\alpha - 4b = 0 \\ O(h^6): &\quad -a + 10\alpha - 16b = 0. \end{aligned} \tag{17}$$

Fourth-order schemes satisfy only the first two equations in (17). Several standard schemes can be expressed in terms of this stencil. If α is set to zero, a fourth-order ''explicit'' scheme results which is denoted E4. Similarly, the original compact fourth-order scheme described in Ref. [8], denoted CD4, is obtained with $b = 0$ (hence $\alpha = \frac{1}{4}$, $a = \frac{3}{2}$) and the stencil consists of only three points $i - \frac{1}{2}$, $i + \frac{1}{2}$, $i + \frac{3}{2}$. A unique sixth-order scheme, CD6, results with the simultaneous solution of Eq. (17), $\alpha = \frac{1}{3}$, $a = \frac{14}{9}$, $b = \frac{1}{9}$. Table I summarizes the coefficients and leading truncation error terms of these and other schemes which will be examined further.

Since these schemes will be applied to practical problems, it is relevant to compare the operation counts of the above compact schemes with MUSCL. For Maxwell's equations, the formation of the dependent variables requires 12 operations for MUSCL (including left and right states), 7 for CD4, and 10 for CD6 and optimized CD4 schemes. When the flux vector operation count is considered, MUSCL requires an additional 30 operations to form and sum the split fluxes while the CD schemes each require only four.

2.4. *Fourth-Order Optimized Schemes*

Schemes that sacrifice rigorous order of accuracy in favor of wide-band performance can provide significantly better wave propagation characteristics in the high wave number range (see, for example, Refs. [4–6]). For this, α may be considered a free parameter, a and b are then expressed in terms of α with the first two of Eqs. (17),

$$a = \frac{2(2+\alpha)}{3}, \quad b = \frac{-1+4\alpha}{3}. \tag{18}$$

It is noted that with $b \neq 0$ the resulting schemes are not strictly compact since the scheme E4 has the same stencil. Nevertheless, the term "compact" is retained to emphasize the implicit nature of schemes with $\alpha \neq 0$. To facilitate Fourier analysis, Eq. (16) may be written in operator notation [17],

$$\begin{aligned} A_1 \cdot \mathscr{V}'_{i+1/2} &= A_2 \cdot \mathscr{V}_{i+1/2}, \quad A_1 \cdot = \alpha\mathfrak{E} \cdot + 1 \cdot + \alpha\mathfrak{E}^{-1} \cdot \\ A_2 \cdot &= \frac{b}{4h}(\mathfrak{E}^2 \cdot - \mathfrak{E}^{-2} \cdot) + \frac{a}{2h}(\mathfrak{E} \cdot - \mathfrak{E}^{-1} \cdot) \end{aligned} \tag{19}$$

where $\mathfrak{E}$ is the shift operator, ($\mathfrak{E} \cdot \mathscr{V}_i = \mathscr{V}_{i+1}$). Thus, the spectral function may be defined as

$$\hat{A}(w) = \frac{A_2 \cdot e^{iws}}{A_1 \cdot e^{iws}} = \frac{i\left(a\sin(w) + \dfrac{b\sin(2w)}{2}\right)}{1 + 2\alpha\cos(w)} \tag{20}$$

in which, following Ref. [4], w is the scaled wave number $w = 2\pi kh/L$ and s is the scaled length $s = x/h$. The number of intervals per wave is then $IPW = 2\pi/w$ and the frequency is $\omega = w/h$. The computed dispersion wave number w_d is related to that of the imposed trial solution w through

$$w_d(w) = \mathrm{Im}(\hat{A}(w)). \tag{21}$$

Alternately, the dispersion wave speed $c_d = w_d/w$ may be employed for analysis. Since $\hat{A}(w)$ is purely imaginary, the discretization is nondiffusive. A scaled isotropy wave number, w_i, may be similarly defined for a wave traveling at angle θ to the mesh [4, 17]:

$$w_i(w, \theta) = \cos\theta w_d(w\cos\theta) + \sin\theta w_d(w\sin\theta). \tag{22}$$

For optimization purposes, the approach of previous efforts is generalized by considering the range, $0 < w < w_{\max}$, where $w_{\max}$ denotes a variable upper wave number of interest. Specifically, an L_1-norm based dispersion error function, E_d, is considered which represents the area between the curves w_d and w:

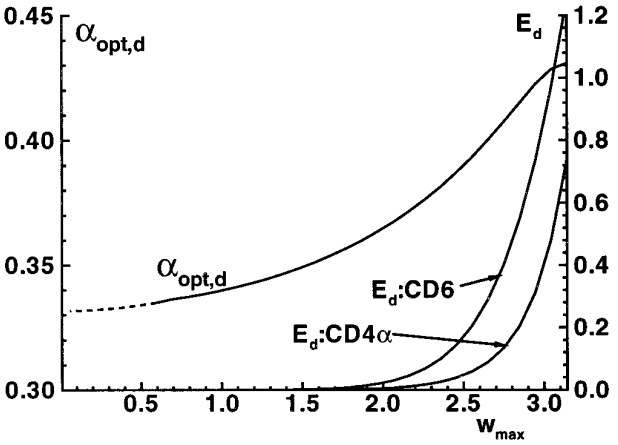

FIG. 2. Variation of dispersion optimized α ($\alpha_{\text{opt},d}$) as a function of wave number range. Also shown are dispersion error functions for a scheme with $\alpha_{\text{opt},d}$ and CD6.

$$E_d(\alpha, w_{\max}) = \int_0^{w_{\max}} |w_d - w|\, dw = \int_0^{w_{\max}} \left| \frac{[2(2+\alpha) + \cos(w)(-1+4\alpha)]\sin(w)}{3[1+2\alpha\cos(w)]} - w \right| dw, \tag{23}$$

where Eq. (18) has been imposed. Alternative expressions and approaches may be found in Refs. [4, 5]. For each value of $w_{\max}$ in $[0, \pi]$, an $\alpha_{\text{opt},d}$ is determined which minimizes the integrated dispersion error, E_d. $\alpha_{\text{opt},d}$ is plotted versus $w_{\max}$ in Fig. 2, together with the error functions $E_d(\alpha_{\text{opt},d}, w_{\max})$ and $E_d(\frac{1}{3}, w_{\max})$ which is the error function for CD6.

Similarly, an isotropy error function is defined

$$E_i(\alpha, w_{\max}) = \int_0^{w_{\max}} \int_0^{\pi/2} |w_i - w|\, d\theta\, dw, \tag{24}$$

where again, $0 < w_{\max} < \pi$ and the integral over θ in Eq. (24) is representative of all angles of wave propagation to the mesh because of symmetry in each quadrant. Values of $\alpha_{\text{opt},i}$ minimizing E_i are plotted in Fig. 3, together with $E_i(\alpha_{\text{opt},i}, w_{\max})$ and the isotropy error of the sixth-order scheme CD6. Note that in both the above error functions it has been implicitly assumed that each wave number is equally weighted. At low values of $w_{\max}$, the evaluation of both integrals is hampered by values near machine accuracy. For this reason, in Figs. 2 and 3, results are extrapolated from higher $w_{\max}$ values. α_{opt} values are bracketed in a narrow range: $0.333 < \alpha_{\text{opt},d} < 0.431$ and $0.333 < \alpha_{\text{opt},i} < 0.408$. Both curves are monotonic and for the same $w_{\max}$, α_{opt} values are slightly lower for isotropy error minimization than for dispersion. In both figures, for low values of $w_{\max}$, $\alpha \to \frac{1}{3}$ which corresponds to the sixth order scheme, CD6 (see Table I). This is not surprising, since in this range all waves are well resolved, or equivalently, the mesh is very fine and the

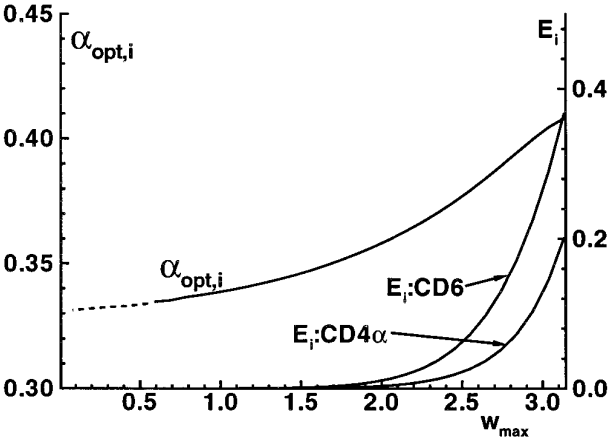

FIG. 3. Variation of isotropy optimized α ($\alpha_{\text{opt},i}$) as a function of wave number range. Also shown are isotropy error functions for a scheme with $\alpha_{\text{opti},i}$ and CD6.

order of accuracy is dictated by the leading term in the truncation error; the $O(h^4)$ term disappears at $\alpha = \frac{1}{3}$ and the most accurate scheme corresponds to the highest order achievable for the given stencil. At higher values of $w_{\max}$, the optimum α deviates from $\frac{1}{3}$ and the family of schemes is denoted "compact" fourth-order optimized, CD4O. At $w_{\max} = \pi$, $\alpha_{\text{opt},d}$ and $\alpha_{\text{opt},i}$ take values of 0.430816 and 0.408277, respectively. Note that if $\alpha > 0.5$, Eqs. (23) and (24) both exhibit singularities at some w and the error is unlikely to be minimized. Finally, operation in the high wave number range $w_{\max} > \pi/2$ is clearly not fruitful because of the rapid growth of error. Figures 2 and 3 show that for any $w_{\max}$, the error functions with the optimized formally fourth-order schemes are lower than with CD6.

In the high wave number range, the leading truncation error term is not the only dominant term; *i.e.*, the algorithm does not necessarily operate in the "linear" convergence range. Rather, cancelation of successive truncation error terms occurs. Consider, instead, of the integral function of Eq. (23), a single wave number w. Transforming the first two terms of the truncation error expansion into Fourier space, cancelation occurs at

$$\alpha(w) = \frac{-42 + 5w^2}{18(-7 + w^2)} \tag{25}$$

which takes the values $\frac{1}{3}$ at $w = 0$ and 0.142 at $w = \pi$. If three terms in the Fourier expansion are considered,

$$\alpha(w) = \frac{1008 - 120w^2 + 7w^4}{27(112 - 16w^2 + w^4)}, \tag{26}$$

which ranges from $\frac{1}{3}$ at $w = 0$ to 0.386 at $w = 2.6$ before dropping to 0.364 at $w = \pi$. The results presented in Figs. 2 and 3 effectively take higher terms into

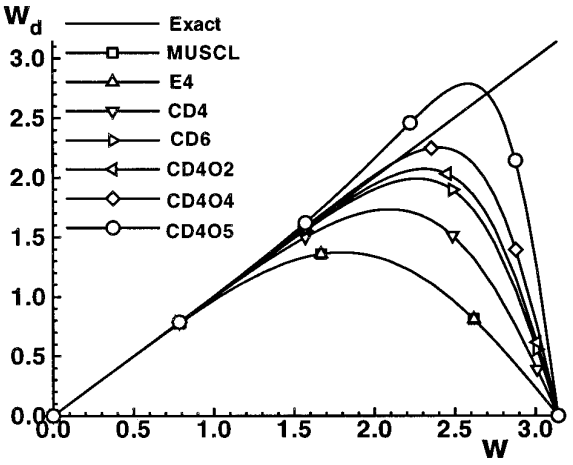

FIG. 4. Dispersion characteristics of semi-discrete schemes. See Table I for key.

account and, in fact, represent minimization of the L_1 norm of the truncation error in Fourier space over the wave number range $0 < w < w_{\max}$ (see Ref. [17]).

Several schemes described in the literature and using the same stencil have α values within the bracket of Fig. 2. For example, the schemes of Ref. [4] correspond to $\alpha = \frac{5}{12} = 0.416667$ and $\alpha = \frac{5}{13} = 0.384615$. Similarly, the *second-order* optimized schemes of Ref. [7] show α in the range between 0.338599 to 0.379389. However, in this case, the corresponding coefficients a and b satisfy only the first of Eq. (17).

To illustrate dispersive and isotropy errors of the above schemes, five α_{opt} values are considered as noted in Table I. CD4O1 and CD4O3 minimize the isotropy error function for $w_{\max} = \pi/2$ and $3\pi/4$, respectively, i.e. where the largest wave number is resolved with 4 and $\frac{8}{3}$ intervals, respectively. Similarly, CD4O2, CD4O4, and CD4O5 minimize the dispersion error function for $w_{\max}$ values of $\pi/2$, $3\pi/4$, and π. The schemes denoted CD4O6 and CD4O7 will be discussed later in the context of the full discretization. The dispersion characteristics of the dispersion-optimized schemes are shown in Fig. 4 in the form w_d versus w, together with those of some of the other schemes of Table I. The exact solution is $w_d = w$. The third-order MUSCL and fourth-order explicit E4 schemes exhibit similar dispersion errors. However, the former has a dominant diffusion term (not shown) consistent with its upwind-biased character. For the same order of accuracy, the compact scheme CD4 is superior to the explicit scheme E4. Large deviation from the exact curve occurs successively later for CD6, CD4O2, and CD4O4, respectively. However, the figure suggests that optimization to very high wave numbers is counterproductive; CD4O5 deviates from the exact significantly prior to CD4O2 or CD4O4. In the high wave number range, with the exception of CD4O5, all schemes show lagging error, i.e. $w_d/w < 1$.

Isotropy characteristics of the schemes are shown in Fig. 5 for the isotropy optimized fourth-order schemes, CD4O1 and CD4O3, together with some of the other schemes in Table I. θ is the angle of wave propagation relative to the mesh while the magnitude of the radial vector is the propagation speed. For the perfect

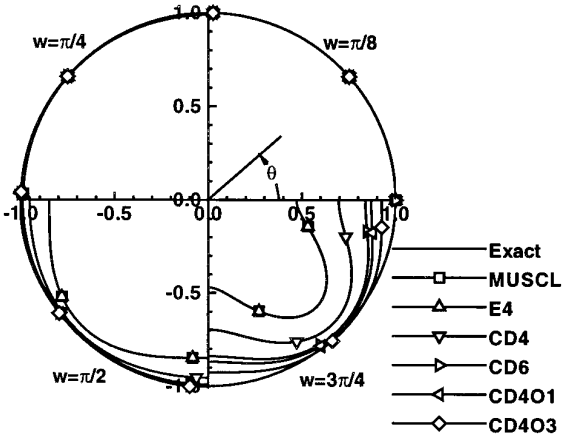

FIG. 5. Isotropy characteristics of semidiscrete schemes. See Table I for key.

scheme, the curve is a unit circle. The four quadrants in this figure are utilized to show isotropy characteristics at four different wave numbers. For well resolved waves, $w = \pi/8$, i.e. 16 intervals per wave; all schemes are quite accurate. As the wave number is increased, there is substantial degradation in MUSCL, E4, and to a lesser extent CD4. Although the distinction between the schemes, CD6, CD4O1, and CD4O3 is relatively small at $w = \pi/2$, these errors can accumulate in problems involving long-time wave propagation. At $w = 3\pi/4$, these differences are clearly evident and, as anticipated, CD4O3 shows the least deviation from the unit circle. All schemes show the commonly observed preferential propagation direction at 45° to the mesh at high w.

2.5. *Order of Accuracy of Pointwise Interface Values*

The use of the above schemes in spatial discretization, based on the primitive function, is now illustrated by a practical examination of truncation error. On $0 < x < 1$, a test function is imposed consisting of a series of unscaled wave numbers, $w/h = 1, 2, ..., 9, 10$ with random phase and unit amplitude. The domain is discretized with a sequence of meshes consisting of 50, 100, 200, 400, 800, 1600, and 3200 intervals. The highest frequency, 10, is thus resolved by 5, 10, 20, 40, 80, 160, and 320 intervals while the support for the lowest frequency is the entire mesh. On the 50-interval mesh, Fig. 6 shows the imposed test function at interfaces as the solid line.

The imposed function is then analytically averaged on each interval to obtain $\bar{u}_i$ at the cell centers. These are plotted as vertical bars straddling the cell center in Fig. 6. The primitive function $\mathscr{V}$ is obtained with Eq. (14) at each interface and is shown in Fig. 7. The derivative of the primitive function is computed with each of the formulas of Table I to obtain high-order estimates of the *pointwise* values of the imposed function at the interfaces. For the present, the boundaries are treated analytically. In Fig. 8, the imposed test function of Fig. 6 is replotted as the analytic curve, together with the computed E4 and CD6 predictions. A close examination reveals larger discrepancies with E4 than with CD6. With the exception of the 50

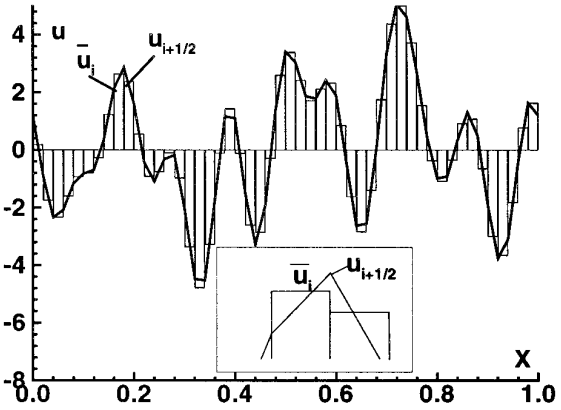

FIG. 6. Test function consisting of 10 frequencies on a mesh with 50 intervals.

and 100 interval meshes, all other discretizations resolve all imposed waves with at least 20 intervals, corresponding to $w = \pi/10$. Linear convergence is thus obtained and regression analysis yields the order of accuracy. This is shown in the L_2 norm of error in Fig. 9. The curves for E4 and CD4 reiterate that for the same order of accuracy compact schemes are more absolutely accurate. The slope of each least squares fit agrees reasonably well with theory. Small deviations are attributable to the nonlinearity of the curve at the coarsest mesh point where the higher frequencies are not in the linear convergence region. On this mesh, the fourth-order optimized schemes have lower absolute error. As the mesh is refined, there is a crossover of CD6 and the CD4O curves as the leading truncation error term becomes more dominant and the spectrum of scaled wave numbers moves to the left in Fig. 2.

3. TIME DISCRETIZATION

Time-integration is achieved with the classical fourth-order four-stage Runge–Kutta method. With R denoting the residual, the governing equation is

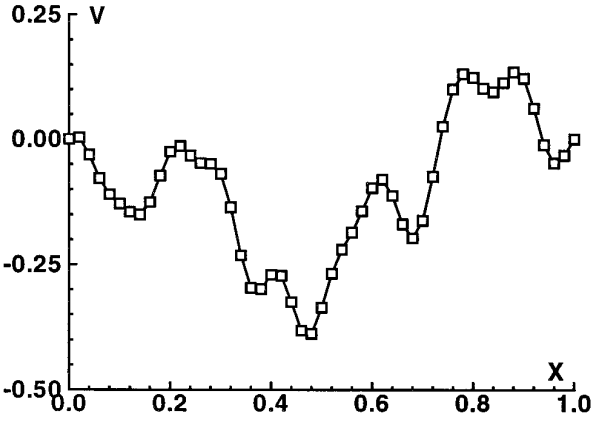

FIG. 7. Primitive function for profile in Fig. 6.

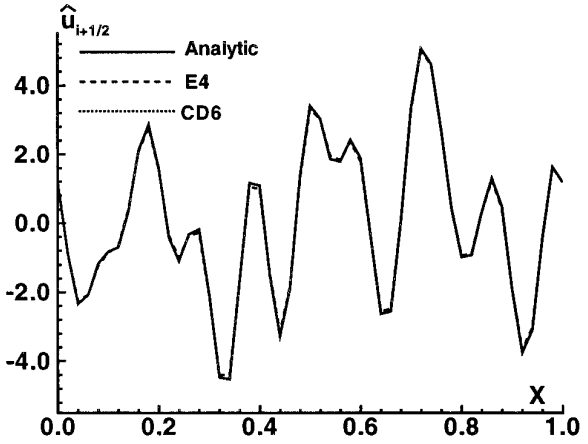

FIG. 8. Pointwise values at interfaces through derivative of primitive function.

$$\frac{\partial \bar{u}}{\partial t} = R.$$

The classical four-stage method may be written as [18]

$$\begin{aligned} k_0 &= \Delta t R(\bar{u}_0), \quad k_1 = \Delta t R(\bar{u}_1), \\ k_2 &= \Delta t R(\bar{u}_2), \quad k_3 = \Delta t R(\bar{u}_3), \\ \bar{u}^{n+1} &= \bar{u} + \tfrac{1}{6}(k_0 + 2k_1 + 2k_2 + k_3), \end{aligned} \tag{27}$$

where $\bar{u}_0 = \bar{u}(x, t_0)$, $\bar{u}_1 = \bar{u}_0 + k_0/2$, $\bar{u}_2 = \bar{u}_1 + k_1/2$, $\bar{u}_3 = \bar{u}_2 + k_2$. The scheme is implemented in the low storage form described in Ref. [19].

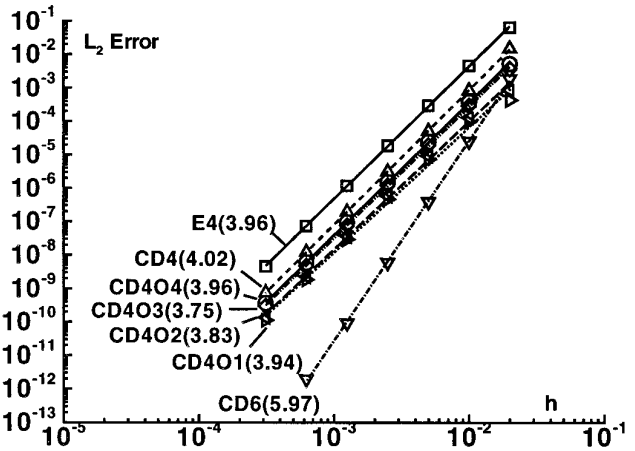

FIG. 9. Order of accuracy of various schemes, the comparison of computed and analytic interface values. Parenthetical values are slopes of least squares fit.

4. ANALYSIS OF FULL DISCRETIZATION

Runge–Kutta methods can be expressed in the form [17]

$$\bar{u}^{n+1} = \sum_{k=0}^{K} \frac{(-\Delta t A\cdot)^k}{k!} \bar{u}^n, \tag{28}$$

where K is the total number of stages and $A\cdot$ is the spatial discretization operator, $A\cdot = A_1^{-1} \cdot A_2\cdot$ (see Eq. (19); the $(-)$ in Eq. (28) appears because of the chosen sign of c in Eq. (7)). In the frequency domain, the complex amplification factor $z(\omega)$ is computed by inserting the spectral function of the spatial discretization operator $\hat{A}(\omega)$ to obtain

$$z(w) = \sum_{k=0}^{K} \frac{(-\hat{A}(w)\,\Delta t)^k}{k!}. \tag{29}$$

Upon substituting $\hat{A}(\omega)$ from Eq. (20) and further replacing a and b with the fourth-order requirement of Eq. (18), the expression obtained is

$$\begin{aligned} z(w, \nu, \alpha) = 1 &- \frac{i\nu(4 + 2\alpha - \cos(w) + 4\alpha\cos(w))\sin(w)}{3 + 6\alpha\cos(w)} \\ &- \frac{\nu^2(4 + 2\alpha - \cos(w) + 4\alpha\cos(w))^2 \sin(w)^2}{2(3 + 6\alpha\cos(w))^2} \\ &+ \frac{i\nu^3(4 + 2\alpha - \cos(w) + 4\alpha\cos(w))^3 \sin(w)^3}{6(3 + 6\alpha\cos(w))^3} \\ &+ \frac{\nu^4(4 + 2\alpha - \cos(w) + 4\alpha\cos(w))^4 \sin(w)^4}{24(3 + 6\alpha\cos(w))^4}, \end{aligned}$$

where ν is the CFL number, $\nu = c\,\Delta t/h$.

The spectrum of semi-discretely developed schemes of Fig. 2 is now examined. For each α, a $\nu_{\max}$ can be determined as the highest value of ν for which $|z| < 1$ for $0 < w < \pi$. $\nu_{\max}$ has been plotted versus α in Fig. 10 as hollow squares.

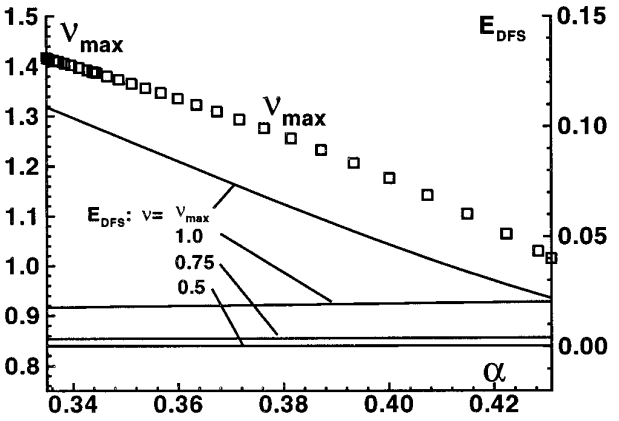

FIG. 10. Maximum CFL (left y-axis) and diffusion error (right y-axis) with RK4.

The maximum CFL number decreases monotonically from 1.42 for the sixth-order scheme ($\alpha = \frac{1}{3}$) to about 1.0 for $\alpha = 0.431$. Clearly, optimization decreases the stability bound. In comparison, the maximum permissible CFL with RK4 for E4 ($\alpha = 0$), CD4 ($\alpha = 0.25$), and MUSCL schemes are 2.06, 1.63, and 1.74, respectively.

The first mode to become unstable is in the vicinity of $w = 2\pi/3$, i.e. at roughly three intervals per wave. For the purposes of further optimization and analysis, therefore, attention is restricted to schemes that can resolve each wave with at least four intervals, i.e. $w_{\max} = \pi/2$. Given this choice, the diffusive error can be characterized by the function

$$E_{\mathcal{DFS},RK4}(\alpha, \nu) = \int_0^{\pi/2} (1. - |z(w, \nu, \alpha)|)\, dw. \tag{30}$$

This diffusion error function is plotted with solid lines in Fig. 10 (right y axis) at several ν values. The curve marked $\nu_{\max}$ is obtained when each of the schemes is operated at its maximum CFL number. The error reduces with increase in α. However, this is dominantly the effect of decreasing $\nu_{\max}$. Since the operation count of each scheme is independent of α, it is more representative to examine the variation of diffusion error at fixed ν. Results with $\nu = 1.0$, 0.75, and 0.5 are plotted in Fig. 10. Diffusion is a much stronger function of ν than of α, especially so at high ν; note the significant reduction in $E_{\mathcal{DFS}}$ from $\nu = 1$ to $\nu = 0.75$, but the relatively smaller improvement at $\nu = 0.5$. Given that the spectral function of the spatial discretization is purely imaginary or nondiffusive for all α, the dominant diffusion characteristic of the algorithm derives from the temporal scheme.

A dispersion error is defined in a manner similar to Eq. (30):

$$E_{\mathcal{DSP},RK4}(\alpha, \nu) = \int_0^{\pi/2} \left| w - \frac{\mathrm{Arg}(z(w, \nu, \alpha))}{\nu} \right| dw. \tag{31}$$

This error is shown for various ν in Fig. 11, where the $\nu_{\max}$ curve has been reproduced. In contrast to diffusion, dispersion errors are not monotonic with either ν or α.

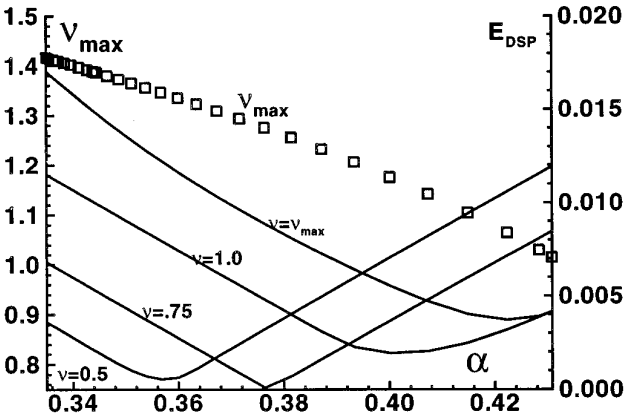

FIG. 11. Maximum CFL (left y-axis) and dispersion error (right y-axis) with RK4.

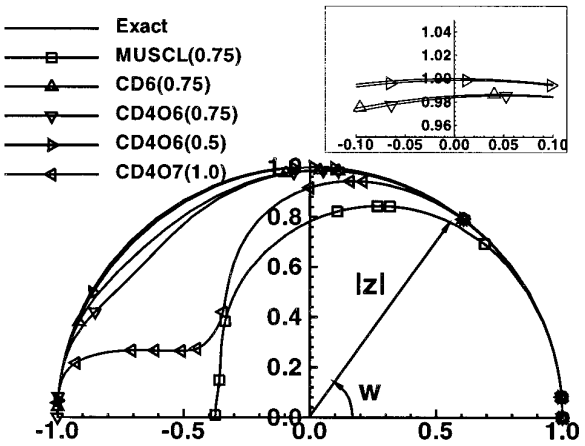

FIG. 12. Amplification factor for various schemes. Numbers in parentheses are values of ν.

When each algorithm is operated at $\nu_{\max}$, a minimum occurs at $\alpha = 0.42$. At constant ν, the minimum occurs at lower values of α. At $\nu = 1$, the least dispersive scheme corresponds to $\alpha = 0.400218$ which is denoted CD4O7 in Table I. At $\nu = 0.75$, a particularly interesting scheme results, CD4O6 with $\alpha = 0.376374$, where the dispersion error is extremely small. With further lowering of ν, the minimum dispersive error occurs at $\alpha \to 0.351075$; i.e. CD4O2 and the properties of the spatial semi-discretization are recovered. Because of the nonmonotonic nature of dispersion error variation, in several ranges the dispersive error actually diminishes with larger ν. This suggests a canceling effect of the temporal and spatial operator dispersive errors similar to that observed for diffusive errors with MUSCL [20].

The amplification properties of some of the above schemes are illustrated in the polar plot of Fig. 12 at a nominal $\nu = 0.75$. Here, the angle formed with the x-axis is w while the magnitude of the radial vector is $|z(w, \alpha, \nu)|$. The MUSCL scheme is clearly very diffusive. For the CD schemes, the dominant factor in diffusion error is clearly the CFL number ν, reiterating the point made with Fig. 10. The relatively high diffusion at high ν is naturally detrimental at wave numbers of interest. However, as demonstrated later, this property can stabilize calculations at high ν. Dispersion errors for the above schemes are plotted in Fig. 13 and reiterate the conclusions outlined in the context of Fig. 11. A relative comparison of the magnitudes of diffusive and dispersive error depends strongly upon ν and is deferred to a later section.

5. EXTENSION TO MULTIPLE DIMENSIONS

A Cartesian coordinate system is chosen to show that the extension to 3D can be achieved by a simple summation of operators in each direction. For a three-dimensional case the average in a cell may be denoted by $\overline{\overline{\overline{U}}}$, where the three overbars denote averages in the three directions, respectively. Reconstruction in the x direction (for example) yields the "line averages" [15], $\overline{\overline{U}}_{i+1/2}$, at each $i + \frac{1}{2}$ interface, where the two overbars denote averages in the y and z directions, respectively. The flux on this interface, by Eq. (4), is

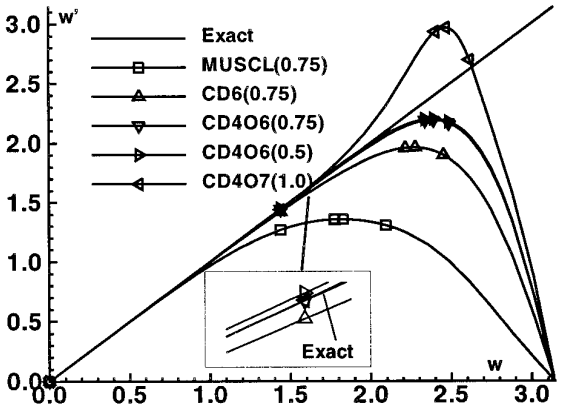

FIG. 13. Dispersion characteristics for various schemes. Numbers in parentheses are values of ν.

$$\iint_{S_{i+1/2}} \Xi \cdot n \, ds = \iint_{S_{i+1/2}} \mathfrak{F} \, dy \, dz. \tag{32}$$

The linear property is now invoked of Maxwell's equations for the subset of electromagnetic problems of interest. If $\mathfrak{F}$ is a linear function of U, say $\mathfrak{F} = \mathscr{A}U$, then the expression for the flux becomes

$$\mathscr{A} \iint_{S_{i+1/2}} U \, dy \, dz = \mathscr{A} \, \Delta y \, \Delta z \overline{\overline{U}},$$

where Δy and Δz are the sides of the $i + \frac{1}{2}$ face. Consequently, a simple summation of operators suffices. This last step is not possible when the system is nonlinear. The extension to curvilinear coordinates may be made in the same fashion as for other FV based schemes. For example, a description for ENO-type procedures may be found in Ref. [15]. The difficulties arising in this endeavor are further discussed in Refs. [9, 21].

6. BOUNDARY CONDITIONS

In the present FV scheme, boundary conditions are applied in two phases. In the first phase, boundary formulas are required to differentiate the primitive function, $\mathscr{V}$, at interfaces $\frac{1}{2}$, $\frac{3}{2}$, $N - \frac{1}{2}$, and $N + \frac{1}{2}$, respectively, where the interior stencil accesses points from outside the domain. In the second phase, the values at interfaces $\frac{1}{2}$ and $N + \frac{1}{2}$ are reset, based on the physical nature of the problem at these interfaces.

It is important to emphasize that boundary conditions have a profound effect on scheme properties, particularly stability [16, 22, 23]. The difficulty of obtaining stable high-order boundary schemes which are "consistent" with the inner scheme, i.e. preserve their formal order of accuracy, has been noted in the literature (e.g., Ref. [24]). Reference [16] contains an extensive and illuminating analysis of some explicit and compact high-order schemes with various boundary formulas. A heuristic stability investigation of the present interior/boundary scheme combinations is presented in Section 7.2 which deals with a boundary-dominated problem.

At interface $\frac{1}{2}$, the form of the compact difference equation may be written as

$$\mathscr{V}'_{1/2} + \alpha_{1/2}\mathscr{V}'_{3/2} = \frac{1}{h}(a_{1/2}\mathscr{V}_{1/2} + b_{1/2}\mathscr{V}_{3/2} + c_{1/2}\mathscr{V}_{5/2} + d_{1/2}\mathscr{V}_{7/2} + e_{1/2}\mathscr{V}_{9/2} + f_{1/2}\mathscr{V}_{11/2}), \tag{33}$$

where the right-hand side of Eq. (33) represents a one-sided formulation with as many undetermined coefficients as are required to obtain a unique formula of sixth order, which is the highest order considered here. The left-hand side maintains the tridiagonal structure of the scheme. Upon matching Taylor series coefficients, a sequence of boundary schemes of varying order of accuracy may be defined. These are summarized in Table II where, for the lower orders, the most compact stencil has been chosen. It is noted that some of these boundary formulas have been reported in the literature (e.g., Refs. [16, 25]).

A similar analysis is applied to the first interface away from the boundary, i.e., $i = \frac{3}{2}$. The basic compact equation is

$$\alpha_{3/2}\mathscr{V}'_{1/2} + \mathscr{V}'_{3/2} + \alpha_{3/2}\mathscr{V}'_{5/2} = \frac{1}{h}(a_{3/2}\mathscr{V}_{1/2} + b_{3/2}\mathscr{V}_{3/2} + c_{3/2}\mathscr{V}_{5/2} + d_{3/2}\mathscr{V}_{7/2} + e_{3/2}\mathscr{V}_{9/2} + f_{3/2}\mathscr{V}_{11/2}). \tag{34}$$

These schemes are summarized in Table III. The conditions required for the right boundary may be derived in a similar fashion and are symmetric in the sense that with the exception of α, the signs of each of the constants is reversed; e.g., the multiplier of $\mathscr{V}_{N+1/2}$ is $a_{N+1/2} = -a_{1/2}$, that of $\mathscr{V}_{N-1/2}$ is $a_{N-1/2} = -a_{3/2}$, etc.

After the interface values are obtained, the states on the boundary are modified to enforce physical boundary conditions. A typical boundary face, e.g. $\frac{1}{2}$ in Fig. 1, is sketched in Fig. 14, where two states are distinguished on either side of the surface. The differentiation of the primitive function yields a state of the solution

TABLE II

Boundary Conditions at Interface $\frac{1}{2}$ for Differentiation of Primitive Function

OA	$\alpha_{1/2}$	$a_{1/2}$	$b_{1/2}$	$c_{1/2}$	$d_{1/2}$	$e_{1/2}$	$f_{1/2}$	TE
6	5	$\frac{-197}{60}$	$\frac{-5}{12}$	5	$\frac{-5}{3}$	$\frac{5}{12}$	$\frac{-1}{20}$	$\frac{-h^6 f^{(7)}}{42}$
5	4	$\frac{-37}{12}$	$\frac{2}{3}$	3	$\frac{-2}{3}$	$\frac{1}{12}$	0	$\frac{h^5 f^{(6)}}{30}$
4	3	$\frac{-17}{6}$	$\frac{3}{2}$	$\frac{3}{2}$	$\frac{-1}{6}$	0	0	$\frac{-h^4 f^{(5)}}{20}$
3	2	$\frac{-5}{2}$	2	$\frac{1}{2}$	0	0	0	$\frac{h^3 f^{(4)}}{12}$
2	1	-2	2	0	0	0	0	$-\frac{h^2 f^{(3)}}{6}$

Note. OA = order of accuracy, TE = leading term of truncation error. Coefficients for $N + \frac{1}{2}$ follow by reversing the signs of all coefficients except $\alpha_{1/2}$.

TABLE III
Boundary Conditions at Interface $\frac{3}{2}$ for Differentiation of Primitive Function

OA	$\alpha_{3/2}$	$a_{3/2}$	$b_{3/2}$	$c_{3/2}$	$d_{3/2}$	$e_{3/2}$	$f_{3/2}$	TE
6	$\frac{2}{11}$	$\frac{-20}{33}$	$\frac{-35}{132}$	$\frac{34}{33}$	$\frac{-7}{33}$	$\frac{2}{33}$	$\frac{-1}{132}$	$\frac{-3h^6 f^{(7)}}{770}$
5	$\frac{3}{14}$	$\frac{-19}{28}$	$\frac{-5}{42}$	$\frac{6}{7}$	$\frac{-1}{14}$	$\frac{1}{84}$	0	$\frac{h^5 f^{(6)}}{168}$
4	$\frac{1}{4}$	$\frac{-3}{4}$	0	$\frac{3}{4}$	0	0	0	$\frac{-h^4 f^{(5)}}{120}$
3					—			
2	$\frac{-1}{2}$	0	0	0	0	0	0	$\frac{h^2 f^{(3)}}{2}$

Note. No third-order scheme is available for chosen compact stencil. Coefficients for $N = \frac{1}{2}$ follow by reversing the signs of all coefficients except $\alpha_{3/2}$.

vector at the boundary face $\frac{1}{2}$. This state is associated with $U^R_{1/2}$, the state in the interior of the domain. The state exterior to the domain, $U^L_{1/2}$ is determined based upon the type of boundary under consideration. Several types of boundary conditions are distinguished.

• *Excitation boundary.* In the total field formulation, the excitation is often introduced at an outer boundary. In this case, $U^L_{1/2}$ is specified by applying an excitation function (ϕ, say) to the appropriate components of the field vector. The split flux is then computed with the formula

$$\mathfrak{F}_{1/2} = \mathfrak{F}^+(U^L_{1/2}) + \mathfrak{F}^-_{1/2}(U^R_{1/2}), \quad \text{where } \mathfrak{F}^\pm = \begin{Bmatrix} 0 \\ \pm\frac{1}{2\sqrt{\mu\varepsilon}} E_y + \frac{1}{2\varepsilon} H_z \\ \pm\frac{1}{2\sqrt{\mu\varepsilon}} E_z - \frac{1}{2\varepsilon} H_y \\ 0 \\ -\frac{1}{2\mu} E_z \pm \frac{1}{2\sqrt{\mu\varepsilon}} H_y \\ \frac{1}{2\mu} E_y \pm \frac{1}{2\sqrt{\mu\varepsilon}} H_z \end{Bmatrix}. \tag{35}$$

This implicitly enforces the condition that there is no reflection of the outgoing wave.

• *Absorbing boundary.* No reflection is specified by setting $U^L_{1/2} = 0$, followed by the application of Eq. (35).

• *Perfect electrical conductor* (*PEC*). The state $U^R_{1/2}$ is modified to reflect the conditions $n \times E = 0$ and $n \cdot H = 0$. Denoting this new state U_{PEC}, the flux is computed as for any interior point, *i.e.* $U^L_{1/2} = U^R_{1/2} = U_{\text{PEC}}$. Note that a split flux

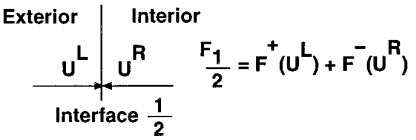

FIG. 14. Schematic of boundary interface for implementation of flux boundary conditions.

may be defined by using $U^L_{1/2} = U_{\mathrm{PEC}}$ and leaving $U^R_{1/2}$ unaltered. Our experience indicates that while this boundary flux-split approach performs better with the MUSCL scheme, i.e. where the fluxes are split throughout the domain, the centered approach is more stable in the present compact centered schemes. In the scattered field formulation, the total field is first constructed at the surface by adding the incident field at the surface. After application of $n \times E = 0$ and $n \cdot H = 0$, the incident field is then subtracted and the flux is computed in a similar fashion.

7. ILLUSTRATIVE EXAMPLES

7.1. *Propagation of a Transverse Electromagnetic (TEM) Polarized Wave in a Homogeneous Isotropic Medium*

The first example discussed is a boundary-free problem designed to highlight the properties of the interior schemes analyzed above. A wave is considered, consisting of a combination of three distinct frequencies (''compact pulse'') represented by the equation [26, 27]

$$\phi = c_\phi(c_{\phi 1} + c_{\phi 2}\cos(\omega_1 t) + c_{\phi 3}\cos(\omega_2 t) + c_{\phi 4}\cos(\omega_3 t)). \tag{36}$$

To obtain a pulse of unit amplitude, $c_\phi = 1/32$, $c_{\phi 1} = 10$, $c_{\phi 2} = -15$, $c_{\phi 3} = 6$, and $c_{\phi 4} = -1$. The frequencies are $\omega_1 = 2\pi$, $\omega_2 = 4\pi$, and $\omega_3 = 6\pi$. The nominal wavelength corresponds to the largest, $\lambda_{\mathrm{nom}} = 1.0$. For TEM excitation, $U = [0, 0, \phi, 0, -\phi, 0]$. The domain is discretized with 38 intervals and the wave travels from left to right. Periodic conditions are applied to simulate continuous propagation over many wavelengths. This results in a periodic tridiagonal matrix for the compact scheme. Since the primitive function is set arbitrarily to zero at interface $\frac{1}{2}$, care must be taken in specifying the wraparound condition. For example, at the left boundary, elements requiring information from the right boundary must be regenerated, e.g., $\mathscr{V}_{-1/2} = \mathscr{V}_{1/2} - h\bar{u}_N$.

Results with several schemes are shown in Figs. 15 and 16 in the form of wave profiles and the L_2 norm of error, respectively, where the latter is computed by comparison of $\hat{\bar{u}}_i$ with the theoretical *average* of the exact solution, $\bar{u}_i$, in each cell. The nominal CFL number ν is 0.75. The MUSCL scheme is marched only $5\lambda_{\mathrm{nom}}$ and shows a large diffusive error. The results with the CD schemes are substantially more accurate even at propagation lengths of $50\lambda_{\mathrm{nom}}$. Although it is difficult to discern relative differences in Fig. 15, several observations of the above analysis are confirmed in Fig. 16: (i) the CD4 scheme is relatively less accurate than the other CD schemes but is substantially superior to MUSCL; (ii) by design, at $\nu = 0.75$, CD4O6 is more accurate than CD6; (iii) CD4O6 is more accurate at

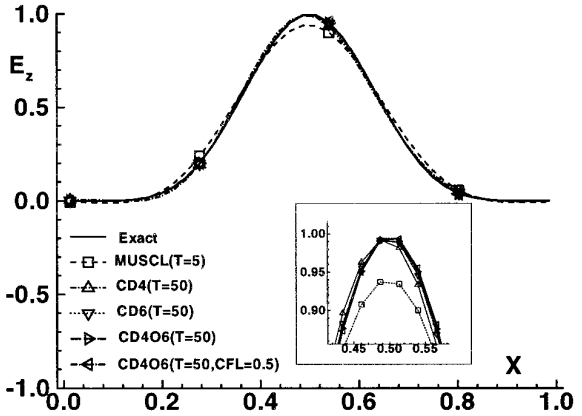

FIG. 15. Propagation of compact pulse with various schemes at a nominal CFL $\nu = 0.75$. T = number of λ_{nom}s traveled.

$\nu = 0.75$ than at $\nu = 0.5$. Although the L_2 norm does not distinguish between diffusive and dispersive error, since diffusion error diminishes with ν (Fig. 10), this result indicates that dispersive error is dominant at these ν values.

The order of accuracy of the full discretization is investigated in Fig. 17 for CD4O6 and CD6 by fixing the time-step size to the small value of $\Delta t = 0.0026$, corresponding to $\nu = 0.1$ on a 38-interval mesh. The formal order of accuracy of the least squares fit is relatively close to the anticipated value. Deviations are attributable principally to the nonlinearity of the curve at the coarsest mesh level and the relatively higher ν on the smaller meshes. The fourth-order scheme is again noted to be superior under conditions of relatively low resolution.

7.2. *Wave Reflecting between PEC Walls*

Boundary conditions can have significant impact on the stability and accuracy properties of the algorithm (see Ref. [28] and the references therein, for example).

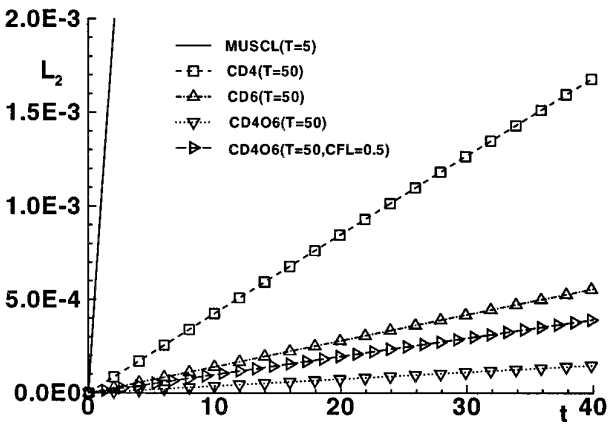

FIG. 16. L_2 norm of error in propagation of compact pulse with various schemes and periodic conditions ($\nu = 0.75$).

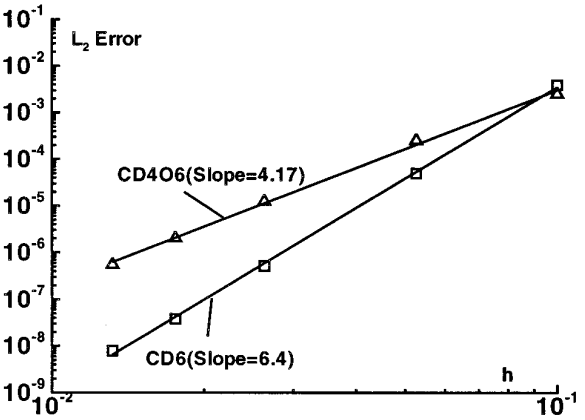

FIG. 17. Order of accuracy for CD6 and CD4O6 schemes with compact pulse. L_2 norm of error at $T = 1$ with $\Delta t = 0.0026$.

Several techniques exist to analyze schemes complete with boundary conditions, including energy and normal mode methods, for example, the GKS analysis of Ref. [22]. For fully discrete multistage algorithms such as RK4, the complexity is enormous [16] although simplifying theories have been proposed to extend semidiscrete results to the fully discrete case for specific time integration methods [23]. The difficulty in analysis is demonstrated in Ref. [16], where it is noted that higher order schemes which are stable in the GKS sense are not necessarily asymptotically or strictly stable. Further, for systems of equations, there are multiple eigenvalues representing wave speeds in both directions. The state derived at each boundary is therefore necessarily based upon downwind information for at least some eigenvalues. Indeed, Carpenter *et al.* [29] note that time-stable schemes for the scalar case are not necessarily so for systems of equations. In the absence of easy to apply analytical tools, a heuristic evaluation of the present family of schemes is presented for a boundary-dominated problem.

For this purpose, the same domain and compact pulse is considered as in the previous case. The right boundary is assumed to be PEC at all times. In $0 < t < 1$, the left boundary is assumed to be an excitation boundary and the pulse enters the domain. This tests the excitation type of boundary condition described above. (Computations starting with the wave already imposed on the domain as an initial condition show similar overall behavior as below.) After the wave enters the domain, at $t = 1$, the left boundary is converted to a PEC boundary to simulate a 1D cavity. The wave then bounces back and forth. At $t = 1, 3, 5, \ldots$, the wave form is centered in the domain on its rightward or incident path while at $t = 2, 4, 6, \ldots$, the form is again centered but on its leftward path. At $t = 1.5, 2.5, 3.5, \ldots$, the incident and reflected waves annihilate each other. The wave form interacts continually with one of the two boundaries.

Following Ref. [16], the notation employed for each spatial discretization is (*a-b-c-d-e*), where *a* through *e* represent the formulas employed, respectively, at interfaces $\frac{1}{2}$, $\frac{3}{2}$, interior points, $N - \frac{1}{2}$ and $N + \frac{1}{2}$. Several of the schemes examined

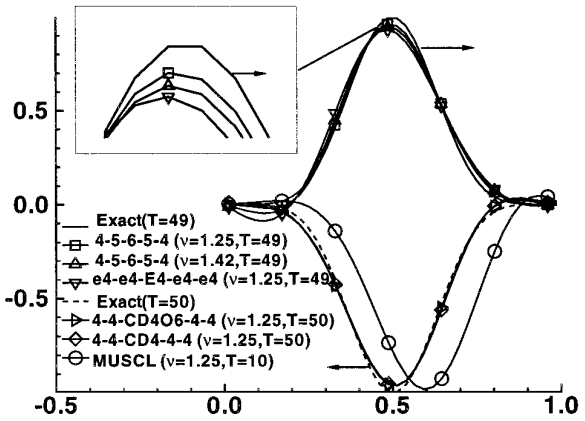

FIG. 18. Wave forms at select times with various stable schemes.

exhibit divergence only after a relatively large number of wave reflections (>5). One such scheme exhibiting a late-time instability is *e4-e4-E4-e4-e4*, where *e4* denotes the explicit fourth-order boundary condition. This completely explicit scheme is GKS stable in the semidiscrete case [16]. Pending further theoretical analysis, for the present it is assumed that a scheme is "practically stable" if the solution does not diverge up to $t \sim 50$; i.e., the wave reflects about 25 times from each boundary.

The results are summarized with the following schemes at various CFL numbers: *6-6-6-6-6*, *5-6-6-6-5*, *4-5-6-5-4*, *4-4-6-4-4*, and *e4-e4-6-e4-e4* in the sixth-order category, and *4-4-CD4O6-4-4*, *4-CD4-4* and the above-mentioned *e4-e4-E4-e4-e4* in the fourth-order category. In the context of lower order boundary conditions for higher order interior schemes, it is relevant to note that the highest formal order of accuracy actually achievable is only one order more than that of the boundary conditions [16, 24]. Figure 18 exhibits the wave form for some of these schemes at $t = 49$ and 50, respectively, when the wave has reflected 48 and 49 times. Figures 19 and 20

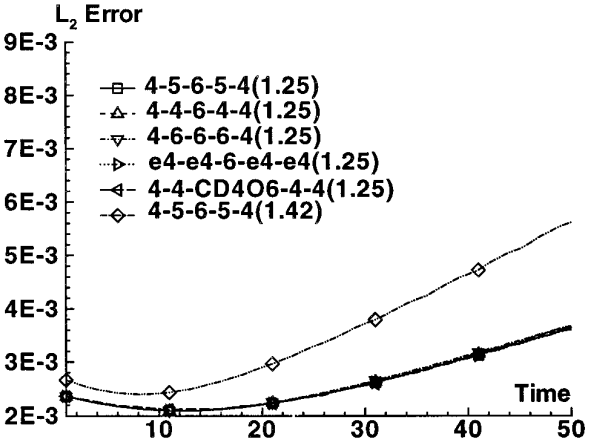

FIG. 19. L_2 norm of error for five-point schemes with various boundary formulations. The quantity in parenthesis is ν.

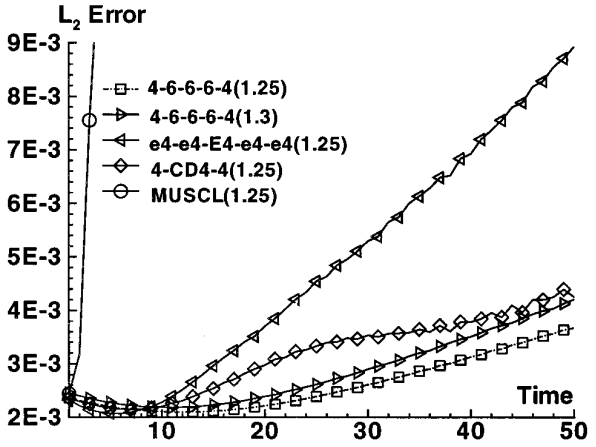

FIG. 20. L_2 norm of error with various five-point schemes, CD4, and MUSCL. The quantity in parenthesis is ν.

display the L_2 norm of error when the wave is at the center of the domain, either on its rightward or on its leftward trajectory. The following observations can be made: (i) The schemes *6-6-6-6-6* and *5-6-6-6-5* exhibit instabilities relatively quickly for all ν values and are, therefore, not plotted in the figures. (ii) Several schemes including *4-5-6-5-4*, *4-4-6-4-4*, and *4-4-CD4O6-4-4*, are stable but only at relatively high values of $\nu \sim 1.25$ but still lower than $\nu_{\max}$. For CD4O6, the stability bound is narrow since $\nu_{\max} = 1.276$. Our experience indicates that the minimum ν for stability is lowered as the mesh is refined. (iii) At these high values of ν, the properties of each stable compact scheme on the five-point stencil is similar at the same ν and the precise boundary formulation is not significant, except that it dictates stability; note the similarity in error of the first five curves in Fig. 19, consisting of CD6 with various boundary formulations. (iv) However, the accuracy is a strong function of ν; note in Fig. 19 the much higher error of *4-5-6-5-4* at $\nu = 1.42$, as compared to $\nu = 1.25$. Coupled with observation (iii) above, this suggests that the diffusion inherent in the temporal operator at these high ν dominates the solution (see Fig. 10). (v) Figure 20 shows that compact schemes employing the five-point stencils, CD6 and CD4O, are superior to the five-point explicit scheme *e4-e4-E4-e4-e4* or the three-point compact scheme *4-CD4-4* scheme at the same ν. (vi) Nevertheless, it is important to note that the absolute error in these schemes is relatively small compared to MUSCL whose error at this ν is predominantly dispersive; Fig. 18 indicates a mean error of less than 5% with most schemes at $\nu = 1.25$ and about 7% at $\nu = 1.42$ after 50 reflections.

7.3. *Dipole*

For a multidimensional case, consider the calculation of the spherical dipole field which has a closed form solution as described in Ref. [12]. The complications in this case arise principally from the $1/r^3$ variation of the field, as well as from the singular lines at the poles of the spherical mesh employed. Analytic continuity

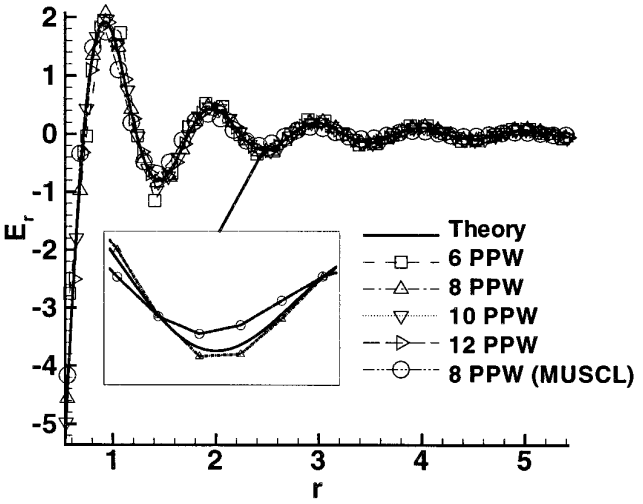

FIG. 21. Dipole solution at $t = 10$, $\phi = \theta = \pi/4$ (PPW = points per wave).

conditions are applied in the latitudinal and longitudinal directions by solving period tridiagonal systems and considering antipodal meridional planes simultaneously. Since the origin is a singular point, the inner boundary is located at a radial distance $r = 0.5$, where the excitation is specified from the analytic solution. The propagation of the signal is examined for scheme *4-5-6-5-4* under various mesh sizes; ν is fixed at the relatively high value of 1.4. Since the smallest time step occurs at the smallest cell which in turn lies at the pole, the major portion of the domain operates at lower effective local ν. The radial component of the electric field strength, E_r, is plotted in Fig. 21 at $t = 10$ for various points per wave, PPW. All the meshes examined correctly reproduce the $1/r^3$ envelope of the signal, the error diminishing consistently with increased mesh resolution. The inset of Fig. 21 shows the superiority of the present scheme to MUSCL at 8 PPW.

8. CONCLUSIONS

A range of high-order compact difference-based finite-volume schemes has been developed for linear wave phenomena. The discretization formula for the interior scheme consists of a five-point stencil. Coefficients are presented which minimize Fourier analysis-based dispersion and isotropy error functions for each wave number range of interest.

This semidiscrete analysis is then refined for the full discretization with the classical fourth-order Runge–Kutta method. Stability bounds are determined and integrated diffusion and dispersion error functions are employed to then optimize the full discretization under the assumption that only waves resolved by at least four or more intervals are of interest. The diffusion error increases monotonically and nonlinearly with CFL number, but it is a weak function of scheme coefficients. At low and moderate ($\sim$0.75) CFL numbers, dispersion error inherent in the spatial discretization is dominant, but it can be minimized for specific Δt by the appropriate

choice of scheme coefficients. Numerical examples with periodic conditions confirm the results of the analysis.

In order to illustrate the effect of boundary conditions, the rapid reflection of a TEM wave between two perfect electrical conducting boundaries is examined. The boundary conditions have a strong influence on the stability of the scheme. This requires the schemes to be run at nonoptimal CFL numbers, where the diffusion characteristics of the time-integration operator dominate. Nevertheless, all the compact five-point stencil operators are superior to five-point explicit, three-point compact, and MUSCL schemes. The extension to multidimensions is tested by the numerical computation of a spherical dipole field.

ACKNOWLEDGMENTS

The authors are grateful for the AFOSR sponsorship by Dr. A. Nachman. The authors acknowledge helpful conversations with M. Aftosmis, J. Casper, and M. Visbal. This work was supported in part by a grant of HPC time from the DoD HPC Shared Resource Centers at Vicksburg, MS, and at WPAFB, OH.

REFERENCES

1. K. S. Yee, Numerical solution of initial boundary value problems involving Maxwell's equations in isotropic media, *IEEE Trans. Antennas Propag.* **14,** 302 (1966).
2. V. Shankar, A. H. Mohammadian, and W. F. Hall, A CFD-based finite-volume procedure for computational electromagnetics—Interdisciplinary applications for CFD methods, *AIAA Paper 89-1987,* 1989.
3. J. S. Shang and D. Gaitonde, Characteristic-based, time-dependent Maxwell equation solvers on a general curvilinear frame, *AIAA J.* **33**(3), 491 (1995).
4. S. K. Lele, Compact finite difference schemes with spectral-like resolution, *J. Comput. Phys.* **103,** 16 (1992).
5. C. K. W. Tam and J. C. Webb, Dispersion-relation-preserving finite difference schemes for computational acoustics, *J. Comput. Phys.* **107,** 262 (1993).
6. C. L. Chen and Y. Liu, Analysis of numerical approaches for acoustic equations, *AIAA Paper 93-4324,* 1993.
7. Z. Haras and S. Ta'asan, Finite difference schemes for long-time integration, *J. Comput. Phys.* **114,** 265 (1994).
8. R. S. Hirsh, Higher order accurate difference solutions of fluid mechanics problems by a compact differencing technique, *J. Comput. Phys.* **19,** 90 (1975).
9. J. Casper, C-W. Shu, and H. Atkins, Comparison of two formulations for high-order accurate essentially nonoscillatory schemes, *AIAA J.* **32**(10), 1970 (1994).
10. B. P. Leonard, *Order of Accuracy of QUICK and Related Convection-Diffusion Schemes,* Technical Report NASA TM 106402 (ICOMP, Cleveland, OH, November 1993).
11. W. H. Enright, Analysis of error control strategies for continuous Runge–Kutta methods, *SIAM J. Numer. Anal.* **26**(3), 588 (1989).
12. R. R. Harrington, *Time-Harmonic Electromagnetic Fields* (McGraw–Hill, New York, 1961).
13. A. Sommerfeld, *Electrodynamics* (Academic Press, New York, 1952).
14. A. Harten, B. Engquist, S. Osher, and S. R. Chakravarthy, Uniformly high order accurate essentially non-oscillatory schemes, III. *J. Comput. Phys.* **71,** 231 (1987).
15. J. Casper and H. L. Atkins, A finite-volume high-order ENO scheme for two dimensional hyperbolic systems, *J. Comput. Phys.* **106,** 62 (1993).

16. M. H. Carpenter, D. Gottlieb, and S. Abarbanel, The stability of numerical boundary treatments for compact high-order finite-difference schemes, *J. Comput. Phys.* **108,** 272 (1993).
17. R. Vichnevetsky and J. B. Bowles, *Fourier Analysis of Numerical Approximations of Hyperbolic Equations,* SIAM Stud. Appl. Math. (SIAM, Philadelphia, 1982).
18. S. D. Conte and C. de Boor, *Elementary Numerical Analysis—An Algorithmic Approach* (McGraw–Hill, New York, 1980).
19. D. J. Fyfe, Economical evaluation of Runge–Kutta formulae, *Math. Comput.* **20,** 392 (1966).
20. Y. S. Weber, Investigations on the properties of a finite-volume, time-domain method for computational electromagnetics, *AIAA Paper 95-1964,* 1995.
21. Y. Liu and M. Vinokur, Exact integration of polynomials and high-order quadratures for finite-volume methods with arbitrary polyhedral grids, in *13th AIAA CFD Conference, June 1997,* Vol. 1, p. 506.
22. B. Gustafsson, H. O. Kreiss, and A. Sundstrom, Stability theory of difference approximations for mixed initial boundary value problems, II. *Math. Comp.* **26,** 649 (1972).
23. H. O. Kreiss and L. Wu, On the stability definition of difference approximations for the initial boundary value problem, *Appl. Num. Math.* **12**(1/3), 213 (1993).
24. B. Gustafsson, The convergence rate for difference approximations to mixed initial boundary value problems, *Math. Comp.* **29**(130), 396 (1975).
25. Y. Adam, Highly accurate compact implicit methods and boundary conditions, *J. Comput. Phys.* **24,** 10 (1977).
26. J. G. Blaschak, *Radiation Boundary Conditions,* Ph.D. thesis, Northwestern University, Evanston, IL, 1988.
27. M. J. Aftosmis, Two Compact Cell-Vertex Methods for Computational Electromagnetics, *AIAA Paper 91-1504,* June 1991.
28. B. Gustafsson and P. Olsson, Fourth-order difference methods for hyperbolic IBVPs, *J. Comput. Phys.* **117,** 300 (1995).
29. M. H. Carpenter, D. Gottlieb, and S. Abarbanel, Time-stable boundary conditions for finite-difference schemes solving hyperbolic systems: Methodology and application to high-order compact systems, *J. Comput. Phys.* **111**(2), 220 (1994).